EUROPEAN ORGANIZATION FOR NUCLEAR RESEARCH

CERN-PPE/92-69
30 March 92

OPTIMIZATION OF CENTRAL PARTICLE TRACKING AT FUTURE HADRON COLLIDERS*

C. D'Ambrosio, T. Gys and H. Leutz
CERN, Geneva, Switzerland

U. Gensch and S. Schlenstedt
Institut für Hochenergiephysik, Zeuthen, Germany

Abstract

Three detector media — gas, semiconductors and scintillating fibres — are compared in view of central tracking at future hadron colliders. As a result of this comparison, we opted for scintillating fibres and propose an optimized tracker arrangement: three cylindrical fibre shells, composed of two straight and two oblique layers each, will cover up to 1.75 rapidity. The individual polystyrene fibre diameters are 60 μm. The computed momentum resolution ranges from 0.3% to 10% for p_t momenta between 10 GeV/c and 1 TeV/c. The vertex resolution along the collider axis amounts to 2.5 mm (for 4° stereo angle). Unwanted contributions like gamma conversions (7%), secondary interactions (5%) and the number of curls per beam interaction are tolerable. Monte Carlo simulations show that occupancy is much less than 1% including curling and secondary tracks and that the fraction of ambiguous track combinations is small. Readout of track images will be performed via an electro-magnetically focused image intensifier with silicon pixels for random access readout. At comparatively slow drifts of the electronic images, it provides an image delay of about 1 μs and can therefore be gated by the first-level trigger of the detector. Consequently, it reduces the readout rate by about three orders of magnitude, thus eliminating most of the minimum bias background.

Submitted to Nucl. Instr. and Methods

---

* The work reported here is part of the LAA Project

1. INTRODUCTION

Future hadron colliders are designed for high energies and luminosities. Their beam parameters, listed for LHC and SSC in table 1, are extremely demanding for the performance of detectors to be installed around the beam crossing points. To meet the physics goals, these detectors will be equipped with calorimeters surrounded by large area muon chambers. The free barrel space of the calorimeter allows for particle tracking, which is vital in a general purpose detector for obvious reasons:

- Momentum measurement of high transverse momentum tracks, in particular for electrons and muons.
- Location of the primary vertex for a triggered event within the multiple vertices of a bunch crossing (fig. 1).
- Provision of topological trigger decisions to enable isolation cuts and to reject minimum bias events.
- Enabling secondary vertex tagging of short lived heavy flavours by linking reconstructed tracks of their decay products to the coordinates obtained via a specially designed vertex detector.

In spite of the increased complexity of the detector, a solenoidal magnetic field would add several advantages to central tracking: it indicates the charge sign of the particles, enables finally momentum measurements and adds therefore credibility to the physics analysis. Moreover, most of the charged tracks from minimum biased events and the majority of decay tracks curl close to the collider axis without barely touching the tracking cells.

In this paper, we discuss the main issues for central tracking at future hadron colliders. We aim first at an optimum choice of the detector medium. Then, we balance different tracking issues to optimize the main parameters of the tracker. For this purpose, we applied, apart from general approximations, Monte Carlo (MC) simulations of pp-interactions at 16 TeV centre-of-mass energy. They were generated with Pythia 5.5 and two event classes were considered: top production (m_{top} = 140 Gev/c^2) and minimum bias events to simulate the always present background. In order to calculate occupancies and to estimate efficiencies for track reconstruction, the generated events were traced through the central tracker by GEANT [1]. Interactions of particles, gamma conversions, multiple scattering, delta ray production, bremsstrahlung and ionization losses within the tracker material were taken into account.

2. MEDIA FOR PARTICLE TRACKING

There exist mainly three different media for particle tracking: gases, semiconductors and scintillators. They all provide signals or hits along the particle path. With subdivisions into adequate detector elements — narrow-spaced wires or strips for gases; strips, pixels or pads for semiconductors, fibres or capillaries for scintillators — these hits indicate space coordinates.

2.1 Gas chambers

Within these three media, only gas detectors provide intrinsic signal amplification. Their mechanism is based on charged avalanches induced by primary electrons in suitable electric field configurations. Their operation relies on well understood technologies and their design allows — within the constraints imposed, if they are operated in magnetic fields (Lorentz angle) — for variations in geometry, gas types and pressures. To achieve the necessary gas amplification, a minimum gas layer of about 2 mm is required, which reflects on their cell size.

The well-established jet and time-projection chambers are inadequate as trackers at future hadron colliders according to their insufficient time and two-track resolutions. Here, we refer only to more recently developed gaseous devices like straw tubes [2], multidrift tubes [3] and microstrip gas avalanche chambers [4-6] which could work in a high-luminosity environment. Straws are cylindrical mylar tubes, with inner conductive layers and anode wires stretched along their axis. Multidrift tubes are modular hexagonal devices. Their individual cells are defined by correspondingly arranged cathode wires, which surround the anode wires, where the avalanche signals are picked up. In the particularly interesting microstrip chamber, about 5 μm to 10 μm wide anode and some 50 μm wide parallel field strips are deposited via UV lithography or plasma etching on an isolating substrate. In this way, cells of about 200 μm pitch and 2 to 3 mm gas depth (cathode distance) are formed. Drawbacks are their sensitivity to magnetic fields (Lorentz angle) and electron drift times between 30 and 50 ns.

2.2 Semiconductors

Detectors based on semiconductors are operated as diodes with reverse bias voltage. Electrons and holes, induced by the passage of ionizing particles, drift within this bias field (~ 300 V mm^{-1}) across the depletion layer, which is, in case of silicon, typically 0.3 mm thick. The charge distribution arriving at the strips or pixels is about 6 μm wide. A magnetic field perpendicular to the drift direction increases this width (at 1.68 Tesla from 6 μm to about 12 μm [7]). The detector elements are geometrically arranged as single or double-sided strips, with typical pitch sizes between 25 μm and 100 μm, and lengths of

several centimetres, or as square or rectangular pixels with edges above 100 μm. All these elements are directly connected, if not bonded or even monolithicaly integrated to their relevant front-end electronics. These electronic channels produce heat, which must be removed by special cooling loops, to avoid a temperature rise of the detector elements leading to increasing leakage currents.

Other semiconductors which can be operated as detector diodes* are GaAs [8] and carbon with diamond structure. Their properties are listed together with those of silicon in table 2(a). Due to its wider band gap, GaAs exhibits a lower intrinsic carrier concentration. In fact, the chance for electrons to be thermally excited into the conduction band is reduced by several orders of magnitudes as compared to silicon. This accounts for thermal noise reduction in pure GaAs wafers. However, the production process of high-purity GaAs wafers is at the time being not as advanced as for silicon. But there are hopes that in a few years time GaAs detectors including GaAs front-end electronics can be produced on a reliable scale. Then, GaAs could provide radiation hard vertex detectors close to the crossing points of future hadron colliders.

With its wide band gap (table 2(a)), diamond structured carbon shows no leakage current and its ionization energy amounts to 13 eV. This reduces its response signal accordingly by three to four times as compared to GaAs or silicon. Natural diamond is contaminated with nitrogen, which reduces the minority carrier lifetime to below 1 ns and makes it difficult as a particle detector. Therefore, diamond structures produced by chemical vapour deposition are preferred, which contain less impurities, are cheaper, but show lattice defects. Although the radiation hardness of diamond is much better than that of silicon, its application as a tracking medium is still far from realistic expectations.

2.3 Scintillating fibres

Particle detection with scintillating organic or inorganic solids and liquids is a well-established method. It has been refined during the last decade by the fibre technique, where scintillating cylindrical cores with diameters ranging from several micrometres up to a few millimetres are surrounded by a cladding layer (~ 5 μm) of lower refractive index. Therefore, the fibre traps by total reflections on its core-cladding interface a small fraction (~ 5%) of the scintillation light, again induced by ionization losses, and guides it via many subsequent total reflections to the fibre end. There, it is in most cases detected by the photocathode of a photomultiplier or an image intensifier.

---

* Hydrogenated amorphous silicon (a-Si:H) based detectors are not adequate for future hadron colliders, since their electron-(~ 1 $cm^2V^{-1}s^{-1}$) and hole-(~0.005 $cm^2V^{-1}s^{-1}$) mobilities prevent them from following the high bunch collision frequency (table 1).

Scintillating fibres might be produced either from glasses with different refractive indices for core and cladding, or from plastic polymers, e.g. polystyrene (PS) for the core and polymethylmetacrylate (PMMA) for the cladding. Instead of solid fibres, also glass capillaries, which serve as cladding, can be filled with scintillating liquids of higher refractive index. In the context of this paper we restrict our considerations for various reasons* to plastic fibres. Some properties of them are listed in table 2(b).

The cell dimensions of a fibre tracker are defined by the lengths and by the diameters of its individual fibres. Since the diametres reflect on its occupancy, its spatial and 2-track resolution, we are interested to keep them small. The lower limit is dictated mostly by reflection losses. These are due to imperfections at the fibres core-cladding interfaces, which cause small reductions from unity ($1 - q \approx 10^{-4}$ to 10^{-5}) for the average total reflection coefficient q [9]. Since the number of reflections increases linearly with decreasing fibre diameters, reflection losses start to contribute noticeably to the total light attenuation somewhere below 100 μm fibre diameter. Therefore, fibre diameters in a tracker must be optimized with respect to spatial resolution and light attenuation. Realistic values range from 30 μm to 100 μm. Such thin fibres must be produced as fused coherent bundles of rectangular cross-sections with edge dimensions between 1 mm and 3 mm [10].

In a fibre tracker, which covers the central region of a particle detector with cylindrical shells of different diameters (figs 2 and 3), each of them is composed of layers with different fibre orientation. Fibres, stretched parallel to the collider axis indicate the (φ, r) coordinates. The two other layers with oblique fibres, running at angles of a few degrees with respect to the parallel ones, provide via their corresponding stereo view the z coordinate of a particle track. In this way, the area to be covered with readout electronics comprises only the endsections of the fibre shells. This results in a tremendous reduction of readout channels as compared to semiconductor detectors, where in contrast a significant fraction of the cylindrical surface of each detector layer must be covered by front-end electronics.

2.4 Comparison of tracking media

Some parameters of the three detector media, with respect to their application as tracking elements in the central detector region, are listed in table 3. As far as feasible, the indicated numbers represent their present state of performance. For valuable comparisons, the numbers given are normalized in the following way:

---

* Radiation length, time resolution, light attenuation (glasses); lower packing fractions and volume variations of liquids with temperature (capillaries).

The number of hits is shown in units of 0.1 radiation length Xo. Heat production and the number of readout channels are indicated in units of subtended surface area [m^2] and hit thickness H, which means the layer of detector material required to achieve one readout signal from the energy loss of a minimum ionizing particle.

Spatial precision means the accuracy to locate a hit within the detector frame. The number listed in table 3 for scintillating fibres is an experimental result and represents the standard deviation (sigma) of a gaussian-shaped hit distribution of a few hundred straight particle tracks [10]. This distribution was measured with 30 μm diameter fibres and it includes the dominating effect of the optoelectronic chain used for this test. With the envisaged new readout (chapter 3.4), this contribution will be reduced and fibre diameters of about 60 μm will achieve similar, if not better spatial precision. For silicon, most experimenters take either the sigma of the centroid (analog readout) or divide the shortest dimension of a detector element by $\sqrt{12}$ (binary readout) to indicate this spatial precision. For gaseous chambers, the spatial precision results from the accuracy with which the centroids of drift clusters can be located.

In contrast, we define the two-track resolution like the classical resolving power in optics, to separate two neighbouring objects (particle tracks). For scintillating fibres the listed number refers to the full width at half maximum of the Gaussian mentioned above. It is therefore related to the spatial precision σ in the usual way: FWHM = 2.36 σ. The two-track resolutions announced in most cases for silicon (≈100 μm) and micro strips gas chambers (400 μm) do not relate in the same way to their spatial precision.

Heat production represents a particular problem of semiconductors. Its smaller fraction is caused by the leakage current of each detector element, but most of the heat originates from the electronics, i.e. preamplifier, shaper, discriminator and pipeline for data storage. It is difficult to estimate a correct number for the power consumption of semiconductors with their inevitable individual readout channels for each element. A cautious estimate leads us to about 0.5 mW per detector element. This heat must be removed by cooling pipes which increase substantially the material layer of such a tracker.

Another important difference is in the readout (see chapter 3.4). Every channel of gas chambers and silicon detectors needs a complete electronic readout chain, including fast front end, discriminator and/or ADC, 67 MHz pipeline and finally a read logic for the events selected by the first level trigger. Fibres are readout at the shell ends and the signal processing, excepting the last read logic, is realized in a passive and parallel way by optoelectronic delay tubes. Consequently, the number of channels is strongly reduced and the electronic readout frequency drops to about 100 kHz (the first level trigger rate).

Using table 3 as a guideline, we have opted for scintillating fibres as detector elements for central particle tracking at future hadron colliders. They constitute a reasonable compromise as far as spatial accuracy and two-track resolution are concerned. Below 100 μm fibre diameter, occupancy is no problem and the number of hits per unit of radiation length is certainly higher than for silicon. Their low number of readout channels is a very important decision criterium. This has of course the consequence, that we must determine the z coordinate along the collider axis via the stereo view α of oblique fibre orientations, like any other strip-detector.

The power of central tracking could certainly be strengthened, if it would be supported by a vertex detector surrounding closely the collider tube. Since radiation hardness is the dominating issue in this context, we would opt for GaAs with pixels of less than 250 μm edge dimension.

3. TRACKING ISSUES

Table 4 lists the most important tracking issues together with their related parameters. In order to design an optimized particle tracker within the free barrel space of the calorimeter, we must carefully balance these parameters to obtain reasonable results for all issues. Since we have opted for a tracker composed of plastic scintillating fibres, table 4 contains only parameters related to this detection mode. This is particularly true for multiple scattering, radiation and interaction length, which are fixed (table 2(b)) and therefore express themselves only in units m of material layer.

3.1 Momentum resolution and vertex pointing

The momentum resolution (δp/p) is composed of two components, the transverse one (index t), which indicates the track curvature in the (r,φ) plane (fig. 2) and the longitudinal one (index //) with polar angle ϑ, indicating the slope in the (r,z)-plane (fig. 3) where the tracks are straight lines for particle momenta ≥10 GeV/c at B=3.3T:

$$\left(\frac{\delta p}{p}\right)^2 = \left\{\left(\frac{G_c}{N}\right)^{1/2} \times \left(\frac{\sigma}{L^2}\right) \times \left(\frac{p \sin\vartheta}{0.3B}\right)\right\}^2_{curv.} + \left\{t^{1/2} \times \left(\frac{0.016 \sin\vartheta}{0.3BL}\right)\right\}^2_{mult.sc.} \Bigg\} p_t$$

$$+ \left\{\left(\frac{G_{sl}}{N}\right)^{1/2} \times \left(\frac{\sigma \cos\vartheta}{L \sin\alpha}\right)\right\}^2_{slope} + \left\{\left(\frac{t}{\sin\vartheta}\right)^{1/2} \times \left(\frac{0.014}{p\,tg\vartheta}\right)\right\}^2_{mult.sc.} \Bigg\} p_{//} \qquad (1)$$

σ[m] means the spatial precision, which is related to the fibre diameter, B[T] the magnetic flux density, L[m] the distance in the (r,φ)-plane between the beam axis and the outermost

measured point (i.e., the radius of the outer shell), t the material layer in units of radiation lengths, α the stereo angle between straight and oblique fibre layers, N the number of hits along the track, G_C a number, which varies between 256 for optimum hit spacing and 720 for continuous hit distribution along the track* [11], and finally G_{SI} which varies in the same way between 2 and 10. The z coordinate emerges from the stereo angle α (see fig. 2).

The momentum resolution calculated for the fibre layout shown in figs 2 and 3 is plotted for three different polar angles in fig. 4. Below 10 GeV/c the resolution is dominated by multiple scattering, and for polar angles below 60°, by the longitudinal momentum contribution. These resolutions have been obtained by using the transversal beam position (±30 μm) as a constraint and by taking N=15 as total number of hits.

The vertex resolution is plotted in fig. 5 for three different stereo angles. It is calculated by a relation similar to (1) for the (r,z)-plane and takes into account the separation of two vertices, i.e. 2.36 times the vertex precision (FWHM). As can be seen from the vertex distribution displayed in fig. 1 for LHC and SSC, the resolution achieved would be sufficient to discriminate between the 15 to 30 vertices produced within one bunch crossing.

3.2 The influence of material layer

The number N of hits increases proportionally to the material layer m of the scintillating fibres. In contrast, the fraction of unwanted gamma conversions, secondary interactions and multiple scattering also increasing with the material layer, should be kept as small as possible. The fraction of converted gammas amounts to:

$$f_\gamma = 1 - e^{-(7m)/(9X_0)} \qquad (2)$$

Most gammas originate from neutral pion decays and therefore their number equals nearly the number of charged minimum-bias particles. A relation similar to (2) holds for secondary interactions, if we consider the interaction length.

According to relation (2), 40 mm of fibre layer, comprising the total tracker thickness, yield 7% conversion fraction and 5% secondary interactions, which agrees fairly well with the corresponding contributions obtained by MC-simulations in fig. 11. The total material thickness in fraction of radiation length results by applying the arrangements and dimensions of fig. 2, and is plotted versus the rapidity covered by our tracker in fig. 6. The parameters of this figure are the different fibre shells including the readout tubes.

---

* In fact, the brackets should read $(720/N+4)^{1/2}$ for this case.

3.3 Tracks curling in a solenoidal field

Let us suppose solenoidal field lines parallel to the collider axis, and that all particles are produced at z = 0 (fig. 3). The number of turns, n_t within the coverage d $\cot\vartheta_{max}$ of our tracker becomes:

$$n_t = \frac{1}{\Delta z}\, d \cot\vartheta_{max} \tag{3}$$

with d being the diameter of the helix and at the same time the maximum distance r of the curling particle from the collider axis. Δz indicates the increment of particle displacement along the collider (z) axis after each helix turn:

$$\Delta z = v_z T = \pi d \cot\vartheta \tag{4}$$

where T means the time needed for a particle starting with velocity v (v_z is its z projection) and polar angle ϑ to accomplish one revolution. Combining relations (3) and (4) and replacing $\cot\vartheta$ by $\sinh\eta$, where η is the rapidity, yields:

$$n_t = \frac{\sinh\eta_{max}}{\pi \sinh\eta} \tag{5}$$

Relation (5) holds in a general way for particles without restriction on their curling diameters (by their absorptions in the solenoid or calorimeter material). These are related to the magnetic flux density B and to the transverse particle momentum p_t:

$$d = \frac{p_t}{0.15\, B} \tag{6}$$

Replacing in relation (5) $\sinh\eta_{max}$ by $Z(r)_{max}/d$ we obtain together with relation (6) for the number of turns:

$$n_t = \frac{0.15\, B}{p_t}\, \frac{Z(r)_{max}}{\pi \sinh\eta} \tag{7}$$

where $Z(r)_{max}$ means the fibre shell length at distance r from the collider axis (fig. 3). Relation (7) is more adequate for calculations based on tracker parameters and indicates that mainly minimum bias particles with low p_t are involved as expected.

According to relations (5) and (7), the number of helix turns would become infinite, if the particle is emitted at zero rapidity ($\vartheta = 90°$). This discontinuity is avoided by decays or interactions of these particles. The number of turns n_d within the decay length l_d of an unstable particle becomes $n_d = l_d/s$ where s means the length of one helix turn:

$$s = \frac{\pi d}{\sin\vartheta} = \frac{\pi p_t}{0.15\, B \sin\vartheta} \tag{8}$$

if we assume again, that the particle is emitted at z = 0 with polar angle ϑ. The decay length can be written:

$$l_d = \frac{p_t c\tau}{m_0 \sin\vartheta} \tag{9}$$

with τ meaning the particle lifetime, m_0 its rest mass and c the velocity of light. Combining relations (8) and (9), we obtain for the number of helix turns within a decay length:

$$n_d = \frac{0.15\ Bc\ \tau}{\pi m_0} \tag{10}$$

Now, if the ratio of relations (5) and (10) becomes unity, we obtain the inversion polar angle ϑ_i above which the curling unstable particles decay inside the tracker:

$$\cot\vartheta_i = \sinh\eta_i = \frac{m_0}{c\tau}\ \frac{\sinh\eta_{max}}{0.15\ B} \tag{11}$$

For charged pions (rest mass: 0.14 GeV/c^2; cτ-length: 7.8 m), which constitute the vast majority of particles in minimum bias events, we obtain for a rapidity coverage of our tracker η_{max} = 1.75 inversion polar angles ϑ_i of 72° or 84.3° for magnetic flux densities of 1 T or 3.3 T respectively. Pions starting with larger polar angles decay within the tracker after 2.6 (at 1 T) or 8.6 (at 3.3 T) turns. For the few longer lived or stable particles the decay length is replaced by the interaction length and similar considerations lead to the inversion polar angle ϑ_i. Taking into account all relations and integrating between $p_t^{min} = 0.15\ B\ r_{in.shell}$ and $p_t^{max} = 0.15\ B\ r_{abs.}$ (absorber: calorimeter or solenoid), the number of helix turns per interaction inside the tracker is shown in fig. 7, together with the average number of interactions per bunch crossing (fig. 8).

3.4 Readout of track images

The readout of fibre signals must preserve their spatial accuracy, their time resolution (< 10 ns) and provide a gating mechanism for the first level trigger to reduce the readout of minimum bias events by some three orders of magnitude. At the same time it should cope with the numerous amount of 60 μm fibres (some 100 millions), since it is hardly possible to read them individually* .

To achieve for our visual signals a 1 μs time delay (required for the first level trigger) by the corresponding travel time of light within optical fibres, would involve an unreasonable optical pathlength (200 m). We therefore decided to first convert at the fibre

---

* Amongst other reasons, this prevents the application of the cryogenic (≈6.5 K) silicon photon counters, which would necessitate the same number of them for our fine grain readout.

ends, via photocathodes, the visual fibre signals into photoelectrons. With this in mind, we designed an electromagnetically focused image intensifier, which covers and reads about (1 to 4) × 10^5 fibre channels (1˝ or 2˝ tube diameter) at a time. Its principle is shown in fig. 9: the image delay is ensured by to and fro drifts of the emitted photo-electrons in the first four sections of the tube. Gating by the first-level trigger occurs when the image in question has arrived on its fro drift after ~ 1 μs trigger delay in the selection section between grids G1 and G2. It is realized within a few nanoseconds by first blocking the photocathode to avoid further image emissions during the gating procedure. This implies a dead time of about 40 ns (0.3%) for each selection procedure, which occurs in LHC every 15 μs on the average. This blockage is immediately followed by a 5 ns negative pulse on grid G1, to kick the wanted image, confined in the selection section, through grids G2 to G5. Finally, the selected image is accelerated at the readout end of the tube.

Electrons emitted from the photocathode have Lambertian angular– and Maxwellian velocity distributions. These distributions reflect on the spatial precision (Lambert) and on the time resolution (Maxwell) of the images. To preserve the required spatial precision, the tube will be oriented parallel to the solenoidal field of the detector. In this way, the electrons drifting with ~ 1 m/μs are spiraling along the magnetic flux lines. Field uniformities as expected for a detector solenoid are more than sufficient for the required spatial resolution of the delay tube. The measured value of it amounts to 25 μm for 0.7 T magnetic flux density [12]. Space charge effects due to the flux of emitted photo-electrons do not noticeably influence the potential distribution in the tube. Calculations based on $10^{34}cm^{-2}s^{-1}$ collider luminosity and 2 mm^{-1} hit density in the fibre shells, show that the transversal potential distribution is only affected by $<10^{-4}$ in the drift zone and by $<10^{-3}$ in the reflection zone.

In case of blue scintillation light incident upon the bialkali photocathode of the delay tube, the Maxwellian energy spread of the emitted photo-electrons can be as high as 1.8 eV. This spread is compensated within the reflection section between grids G3 and G4, since faster electrons penetrate farther into this section and therefore take longer to return. In this way, we obtain the bunching condition:

$$D/d = 2 \times (E'/E)^{1/2}$$

where D means the distance between G1 and G3, d that between G3 and G4, and E or E' the maximum or minimum energies of the accelerated electrons (after G1). With such a design, the delay tube achieves a measured time resolution of better than 10 ns within the selection section.

In the last section (G5) the selected electron-image is accelerated to 25 keV and hits at the readout a silicon pixel detector (pixel size> 600 μm (r) × 60 μm (φ)) placed inside the delay tube. The image is finally read out by random access, which addresses only the occupied pixels within some microseconds, thus enabling track information for the second level trigger.

3.5 Radiation levels

The radiation levels of the three tracker shells would amount to 0.75 kGy (R=0.75 m), 0.43 kGy (R=1 m) and 0.25 kGy (R=1.3 m) for an integrated luminosity of 10^{41} cm^{-2} or one year of operation at 10^{34} $cm^{-2}s^{-1}$ luminosity. Taking into account curling tracks at 3.3 T magnetic flux density, these levels change to 0.9 kGy, 0.25 kGy and 0.05 kGy, respectively. Albedo neutrons (2×10^{13} cm^{-2} [13]) would increase these radiation levels by ≈20% (inner shell) and ≈100% (outer shell).

3.6 Tracking simulations

The occupancy O means the fraction of occupied cells with respect to the total number of tracker cells. It is proportional to the collider luminosity $\mathcal{L}$, the cross-section σ of colliding particles, the number n_η of minimum bias particles per unit of rapidity η and per interaction and to the time t_b between two bunch crossings.

Apart from these collider parameters, we have also to take into account those of the detector elements. These are: their radial distance r from the collider axis, the rapidity range η_{max} they cover and their transverse cell dimension s (perpendicular to r):

$$O = (L \sigma n_\eta t_b) \times \left(\frac{s \eta_{max}}{2\pi r} \right) \qquad (12)$$

When the cell busy time t is longer than t_b, then (12) has to be multiplied by t/t_b *.

Inserting the appropriate quantities, relation (12) yields a first approximation, which does not take into account particles curling in the magnetic field, production of secondaries and delta rays, bremsstrahlung and shower production of electrons, and neutral pion decays with subsequent gamma conversions. Therefore, we computed the occupancies also via MC-simulations described in the introduction. Some occupancies are plotted in fig. 10 for fibre diameters of 0.06 mm and 1 mm and for various magnetic flux densities versus the distance of tracker shells from the collider axis. For comparison, occupancies calculated from relation (12) are also indicated (luminosity: 10^{34}, cross-section: 100 mbarn, 6 particles per unit of rapidity and η_{max}=1.35).

---

* For the system described, we take t/t_b=1

For track finding we must associate to the azimuth hits in φ their symmetric u and v-hits (fig. 2). According to table 4, the stereo angle α must carefully be chosen to balance the z precision against the angle β, which should be kept reasonably small to avoid confusion for track finding. Obviously, also increasing occupancies generate ambiguities, which fake u_i,v_i symmetries with respect to radial φ_i-tracks by u- and v-hits not really associated to the central φ-hits but satisfying the following conditions:

$$(u_i + v_i)/2 = \varphi_i \qquad \text{and} \qquad (u_i - v_i)/2 = \beta_i \tag{13}$$

How many (u_j,v_k)-doublets exist at a certain occupancy O, which satisfy relations (13), but do not belong to the central φ_i-track and therefore simulate ghost tracks ?

The total number of u plus v tracks in a given β_{max} interval* of a fibre shell section can be written:

$$N_{tot}^{\beta max} = \left(\frac{\beta max}{2\pi}\right) \times 2N_{tot} = \left(\frac{\beta max}{2\pi}\right) \times \left(\frac{2\pi r}{\varnothing}\right) \times 2O \tag{14}$$

with N_{tot} meaning the number of charged tracks inside the tracker per bunch crossing**. To obtain the number of ambiguous (ghost) tracks we subtract from this total number all "single" tracks, i.e. all u- and v-tracks missing a symmetric partner (with respect to a central φ-hit) in the corresponding u or v-layer. For these configurations we obtain $2P_0P_1$, with (P_0,P_1) indicating the Poisson probability for zero or one track segment respectively. Extending this to (P_0,P_n) and multiplying by n , we obtain the fraction F for all possible u,v-combinations missing a symmetric partner:

$$F = 2P_0 \sum_{n=1}^{\infty} n P_n = 2P_0 O\, e^{-O} \sum_{n=1}^{\infty} \frac{O^{n-1}}{(n-1)!} = 2P_0 O \tag{15}$$

if we substitute P_n by $(O^n e^{-O})/n!$ and calculate the series. This procedure leads to the number of "single" tracks, within the angular interval $\pm\beta_{max}$ of our fibre shell section:

$$N_s^{\beta max} = \left(\frac{r\beta max}{\varnothing}\right) \times 2P_0 O \tag{16}$$

The number of (u,v)-doublets symmetric to their φ-signatures within $\pm\beta_{max}$ results finally by substracting relation (16) from relation (14):

$$\frac{1}{2}\left(N_{tot}^{\beta max} - N_s^{\beta max}\right) = \left(\frac{r\beta max}{\varnothing}\right) \times O(1 - P_0) = \frac{N_{amb}}{N_{tot}} \tag{17}$$

---

* $\beta_{max} = \sin\alpha \sinh\eta_{max}$ with η_{max} meaning the rapidity coverage of half a fibre shell (fig. 2).

** $N_{tot} = \mathcal{L}\, \sigma\, n_\eta\, \eta_{max}\, t_b = O\,(2\pi R/\varnothing)$ (see relation (12), with $\varnothing$ replacing s).

which equals the fraction of ambiguous track segments N_{amb} (ghosts) from the total number of tracks N_{tot} within the tracker.

In order to take into account a safe two track separation, we introduce the quantity n_c, indicating the number of detector cells (fibre diameters) we consider necessary to define a track "corridor". Then, relation (17) can finally be simplified for occupancies smaller than ≈ 30%* :

$$\frac{N_{amb}}{N_{tot}} = \left(\frac{r\beta_{max}}{\varnothing}\right) n_c O^2 = \left(\frac{\beta_{max}}{2\pi}\right) \times \left(\frac{\varnothing}{2\pi r}\right) \times n_c N_{tot}^2 \qquad (18)$$

For occupancies O<0.01, O must be substituted by $O - (\varnothing/2r\beta_{max})$.

Relation (18) shows a linear dependence on β_{max} which in turn is connected to the rapidity η_{max} covered by half a fibre shell and to the stereo angle α between the straight φ-fibres and the oblique u- or v- fibres. The most important quantity is the occupancy of the tracker shell, which must be kept certainly below 1% to avoid too many ambiguities. Fig 12 shows the fraction of ambiguous tracks for different tracker layouts. From these figures it can easily be seen that this fraction increases drastically with the fibre diameter. By linking the φ-segments of n different fibre shells, the fraction of ghosts would roughly follow the relation $(N_{amb}/N_{tot})^n$. This holds, for example, for shells constructed with slightly different stereo angles and therefore uncorrelated ghosts and for fractions smaller than unity.

4. CONCLUSIONS

As medium for a particle tracker to be implemented within the free barrel space of the detector calorimeter, we have opted for scintillating plastic fibres [14]. According to table 3, this represents a compromise between hit density per radiation length, multiple scattering, two-track resolution, number of readout channels, and heat production in favour of fibres and spatial precision in favour of silicon. Occupancy does not play a role for both techniques. Gaseous devices are restricted by their cell busy times and by their occupancy.

The shell radii chosen present also a compromise between radiation exposure, which asks for detector components as distant from the collider axis as possible, and the area of the shell end sections which must be covered by opto-electronic delay tubes. Fortunately, the radiation level decreases with r^2, but the readout area increases only linearly. The empty space between the fibre shells looks very inviting to be filled up with

---

* $1\text{-}Po = O\text{-}O^2/2+O^3/3!\text{-}....$

other detector components. If at all, this should be considered with great care, in particular in view of the additional material layer.

To conclude, the fibre tracker which emerged from our optimization procedure, shows the following design parameters: fibre arrangement in three shells with dimensions as indicated in figs 2 and 3. Stereo angle between oblique and straight fibre layers of 4 degrees, which enables nearly 98% of φ, u and v triplet identification for 60 μm fibre diameter. At the same time, the fraction of fake (ghost) tracks is reduced to about 2%. Momentum resolutions better than 3% below 100 GeV/c transverse momentum (fig. 4) can be achieved with 60 μm fibre diameter. This diameter represents a compromise between spatial precision σ (relation (1)) on one side, and reflection losses and packing fraction* on the other side. For hexagonal arrangement of the fibres, the packing fraction improves from 73% for 30 μm fibres to 85% for 60 μm fibres and reaches 90% for 90 μm fibres. Occupancy is well below 1% for the arrangement chosen. Work is going on to further improve the hit density of the plastic fibres, which could still decrease the material layers of the fibre shells. This can be achieved by applying new dopants [15] dissolved in the polystyrene cores of the fibres and new claddings of lower refractive index [16]. Finally, the delay tube will provide fast triggered readout with excellent spatial precision and time resolution.

ACKNOWLEDGEMENTS

We wish to thank Prof. A. Zichichi for his continuous interest and support of our work. We also acknowledge substantial support from Dr F. Cindolo and technical assistance from D. Piedigrossi and S. Tailhardat.

---

* Packing fraction means the ratio between the fibre core cross section and the fibre (core + cladding) cross section . It is included in all our considerations for hit densities.

REFERENCES

[1] R. Brun et al., GEANT3, CERN Program Library Long Writeup, W5013.

[2] G. Hanson, M. Cundy and A. Palounek, Nucl. Instr. and Meth. A 289 (1990) 365.
G. Hanson, B. Niczyporuk and A. Palounek, SLAC PUB–4805 (1988).

[3] R. Bouclier et al., Nucl. Instr. and Meth. A 283 (1989) 509.

[4] A. Oed, Nucl. Instr. and Meth. A 263 (1988) 351.

[5] F. Angelini et al., Nucl. Instr. and Meth., A283, (1989) 755

[6] F. Udo, proc. of the Large Hadron Collider Workshop, CERN 90–10, Vol 3 (1990) 219.

[7] E. Belau et al., Nucl. Instr. and Meth. A 214 (1983) 253.

[8] R. Bertin et al., Nucl. Instr. and Meth. A 294 (1990) 211.

[9] C. D'Ambrosio et al., Nucl. Instr. and Meth., A306, (1991) 549.

[10] H. Leutz, proc. of the ECFA Study Week on Instrumentation Technology for High-Luminosity Hadron Colliders, CERN 89–10 (1989) 176.

[11] R.L. Gluckstern, Nucl. Instr. and Meth. 24 (1963) 381.

[12] T. Gys et al., proc. of the ECFA Study Week on Instrumentation Technology for High-Luminosity Hadron Colliders, CERN 89–10 (1989) 255.

[13] G.R. Stevenson, proc. of the Large Hadron Collider Workshop, Aachen, Germany, CERN 90–10, vol.III (1990) 566.

[14] C. D'Ambrosio et al., CERN-PPE/92-26, CERN/LAA/SF/91-25.

[15] C. D'Ambrosio et al., Nucl. Instr. and Meth., A307, (1991) 430.

[16] C. D'Ambrosio et al., to be published.

FIGURE CAPTIONS

Fig. 1 Vertex distributions per bunch crossing along the collider (z)-axis for LHC and SSC. z = 0 means the nominal bunch crossing point for the detector in question, the opposite z direction is symmetric. The integrated values are 15 and 14 vertices per bunch crossing for LHC and SSC, resp. For other luminosities multiply the ordinate with the corresponding factor.

Fig. 2 Arrangement of scintillating fibre shells for tracking within the free barrel region of the calorimeter. r–φ plane seen at z = 0. The magnified parts show the subdivision into the straight φ and the oblique u and v layers. The symmetric angles β indicate the z coordinate via the indicated relation.

Fig. 3 r–z plane. The tracker covers up to 1.75 rapidity. Readout with electromagnetically focused delay tubes is at z = 0 of each shell. ϑ means the polar angle.

Fig. 4 Momentum resolution versus momentum in a solenoidal field of 3.3 T magnetic flux density. The assumed hit distribution corresponds to the arrangement of figs 2 and 3. For the 60 μm fibres, the resolution is dictated below 10 GeV/c by multiple scattering (dashed curves for a) and b)).

Fig. 5 Vertex resolution achieved with the oblique v and u layers at the indicated stereo angle α. The assumed hit distribution corresponds again to the arrangement of figs 2 and 3. This resolution must be compared to the vertex distribution in fig. 1.

Fig. 6 Material layers of the fibre tracker in fractions of radiation lengths versus the rapidity η. The shell thicknesses are indicated in fig. 2. For the readout tubes we took ceramic (radiation length : 7.65 cm; density : 3.65) walls of 1 mm thickness,which is multiplied by π for the average thickness and by 4/7 to account for their filling factor.

Fig. 7 Number of curls hitting the fibre shells arranged at the indicated distances (shell radii) from the collider axis versus the magnetic flux density of solenoidal fields oriented parallel to this axis. The number is calculated per beam interaction following relation (12), taking into account the p_t distribution of minimum-bias events (fig. 8), decaying (relation 10) and interacting particles. It must be emphasized that the vast majority of the curl lengths occurs between the fibre shells and hits are only seen at crossing points with fibre shells.

Fig. 8 Average number of interactions per bunch crossing versus the collider luminosity. To obtain the number of curls per bunch crossing for a certain luminosity, the corresponding ordinate values of figs 7 and 8 must be multiplied. The insert shows the p_t distribution of minimum-bias events used for fig. 7.

Fig. 9 Scheme of delay tubes to read out the track images. Typical grid potentials and the field direction of the detector's magnetic flux density are indicated and the sequence of electronic pulses released by the first-level trigger is displayed.

Fig. 10. Occupancies of tracker shells versus the shell radius generated by M.C.-simulations with Pythia 5.5 and GEANT (see text). For comparison, the occupancies calculated according to the relations in chapters 3.3 and 3.6 are also displayed.

Fig. 11 Different contributions piling up to the total occupancy of minimum bias events per bunch crossing at 10^{34} luminosity for the inner, centre, and outer shells of the tracker composed of 60 μm diameter scintillating fibres.

Fig. 12 Fraction of ambiguous (ghost) tracks calculated from rel. (18) for one fibre shell. The simulated occupancies (fig. 10), track corridor n_c=3 and β_{max} for ±4° stereo angle and 1.35 rapidity are taken into account. For comparison, the fraction for 1 mm fibres and ±16° stereo angle is also displayed. It is obvious, that small diameter fibres and well balanced stereo angles are essential to obtain sufficiently low fractions of ghost tracks. For small ambiguities and if the stereo angles are slightly different for each shell, their fractions must be brought to the power of n, where n is the number of fibre shells .

Table 1 Parameters of colliding beams at future hadron colliders

BEAM PARAMETERS		LHC	SSC
Full beam crossing angle	μrad	200	0–150[a]
Beam diameter (4 σ = 95% of particles)[c]	μm	42	19.2[b]
Bunch length (4 σ = 95% of particles)[c]	m	0.31	0.24
Depth of focus (β*)	m	0.5	0.5
Length of luminous region (95% of interactions)[c]	m	0.19	0.15[d]
Bunch crossing time (95% of interactions)[c]	ns	0.63	0.5
Bunch separation	ns (m)	15 (4.5)	16.7 (5.0)
Bunch collision frequency	s^{-1}	66.7×10^6	60×10^6
Luminosity	$cm^{-2}s^{-1}$	10^{34}	10^{33}
Average number of vertices		15	1.4

(a) adjustable

(b) $\beta^* = 0.5$ m

(c) for 68% divide by two

(d) crossing angle = 75 μrad

Table 2(a) Properties of semiconductors*

		Si	C	GaAs
General properties				
Atomic number		14	6	32 (average)
Atomic weight		28.09	12.01	144.63
Crystal structure		Diamond	Diamond	Zinkblende
Lattice Constant	nm	54.31	35.67	56.53
Number of atoms	cm^{-3}	5×10^{22}	1.8×10^{23}	4.42×10^{22}
Density	$g\ cm^{-3}$	2.328	3.515	5.318
Melting point	K	1693	4100	1513
Thermal conductivity	$W\ cm^{-1}K^{-1}$	1.5	20	0.45
Linear expansion coefficient	K^{-1}	1.6×10^{-6}	10^{-6}	6.86×10^{-6}
Electrical properties				
Energy gap	eV	1.12	5.48	1.428
Specific dielectric constant		11.9	5.66	12.73
Intrinsic carrier concentration	cm^{-3}	1.45×10^{10}		1×10^{7}
Intrinsic resistivity	Ωcm	2.3×10^{5}	(10 to 10^{4})	10^{8}
Mobility of electrons	$cm^2V^{-1}s^{-1}$	1500	1800	8000
Mobility of holes	$cm^2V^{-1}s^{-1}$	480	1200	400
Breakdown field	$V\ cm^{-1}$	3×10^{5}	$> 10^{6}$	4×10^{5}
Minority carrier lifetime	s	2.5×10^{-3}	$\leq 1 \times 10^{-9}$	10^{-8}
Ionization energy	eV	3.6	~ 13	4.2
Radiation properties				
Radiation length	cm	9.36	12.15	2.3
Gamma conversion length	cm	12.03	15.6	3.0
Nuclear interaction length	cm	45.53	24.55	26.4
(dE/dx) min	MeV/cm	3.87	6.26	7.44
Multiple scattering angle (1 GeV/c; 1 mm material)	mrad	1.551	1.36	3.12

* Values compiled by F. Pengg [private communication].

Table 2(b) Properties of polystyrene

General properties		
Average atomic number		3.5
Density	g cm^{-3}	1.03
Proton/Neutron ratio		1.17
Melting point	°C	240
Thermal conductivity	W $cm^{-1}K^{-1}$	0.105
Linear thermal expansion coeff.	K^{-1}	7×10^{-5}
Tensile modulus (E)	MPa	3200
Dielectric constant		2.5
Optical properties		
Refractive index		1.59 (590 nm) 1.58 (480 nm)
Optical dispersion	ns m^{-1}	0.04 (400 nm to 500 nm)
Light decay (1/e)	ns	2 to 3 (depending on dopant)
Light velocity in PS	m ns^{-1}	0.21
Numerical aperture		0.53 (n cladding = 1.49) 0.69 (n cladding = 1.42)
Photon yield	$(keV)^{-1}$	~ 10 (depending on dopant)
Radiation properties		
Radiation length	cm	42.4
Gamma conversion length	cm	54.5
Nuclear interaction length	cm	79.6
Multiple scattering angle	mrad	0.73 (1 GeV/c; 1 mm PS)
(dE/dx) min	MeV/cm	2.0

Table 3 Comparison of relevant detector parameters between different detector media. X_0 means radiation length and H the material layer required to achieve 1 hit.

Parameters		Silicon	Fibres	Gas[a]
Number of hits	$(0.1\ X_0)^{-1}$	15–30[b]	42–63[c]	~10-15[d]
Occupancy ($10^{34}cm^{-2}s^{-1}$ luminosity)	%	< 1	< 1	2-3[d]
Multiple scattering mrad	$(GeV)^{-1}\ H^{-1}$	1.1	0.7	1.4
Cell busy time	ns	5	3	30–50
Spatial precision	μm	7[e]	35	40
2-track resolution	μm	100	80	400
Number of channels	$m^{-2}\ H^{-1}$	4×10^6[f]	1×10^4[g]	4×10^4[h]
Heat production[i]	$W\ m^{-2}\ H^{-1}$	5×10^3	1[k]	~200

(a) Micro-strip gas chambers. Occupancy and 2-track resolution for other gaseous devices are too large.

(b) 0.3 mm detector + 0.3 mm electronic layer per hit, higher number without electronics.

(c) 1 (0.75) mm polystyrene fibre per hit

(d) Arrangement of F. Udo et al [6] and Angelini et al., CERN-PPE 91-122.

(e) Silicon strips with 25 μm pitch, divided by $\sqrt{12}$.

(f) Silicon element of 25 μm pitch and 1 cm strip length.

(g) 10 000 pixels of 60 μm × 600 μm each, at the readout end of one delay tube. They cover 3.6 cm^2 of fibre endsections. For 1 mm fibre layer (hit thickness H) this corresponds to 7.6% of shell circumference (at 0.75 m radius). With 2.1 m shell length (1.75 rapidity), one tube covers $2.1 \times 2\pi \times 0.75 \times 0.076 = 0.75\ m^2$. This increases to 1 m^2 for H = 0.75 mm. The mean value is indicated.

(h) Arrangement of F. Udo et al [6]. One ring of MSGC needs 2.8×10^5 channels (F. Hartjes). 20 rings cover about 12 m^2 and provide 12 hits on the average.

(i) Assuming 0.5 mW per channel.

(k) Delay tube pixels will only be activated by the first-level trigger.

Table 4 List of tracking issues, which improve with the indicated parameters and related inconvenient effects, which increase with the indicated parameters.

Tracking issues	improving with	Inconvenient effects	increasing with
Momentum resolution	ϕ^{-1}, $\sqrt{m}$, B	secondary interactions	m
Vertex location (z)	ϕ^{-1}, $\sqrt{m}$, α	gamma conversions	m
Occupancy	ϕ^{-1}, r, η^{-1}	multiple scattering	$\sqrt{m}$
Track finding	ϕ^{-1}, m, α^{-1}, β^{-1}	number of turns for curling tracks	B, η
Track reconstruction prob.	ϕ^{-1}, α^{-1}, β^{-1}	number of readout channels	r
Radiation damage	r^2		

ϕ: fibre diameter

B: magnetic flux density

m: material layer of detector

η: rapidity

r: shell radius or distance from collider axis

α: stereo angle of oblique u and v layers

β: angular range to find u and v hits symmetric to φ hits (fig. 2)

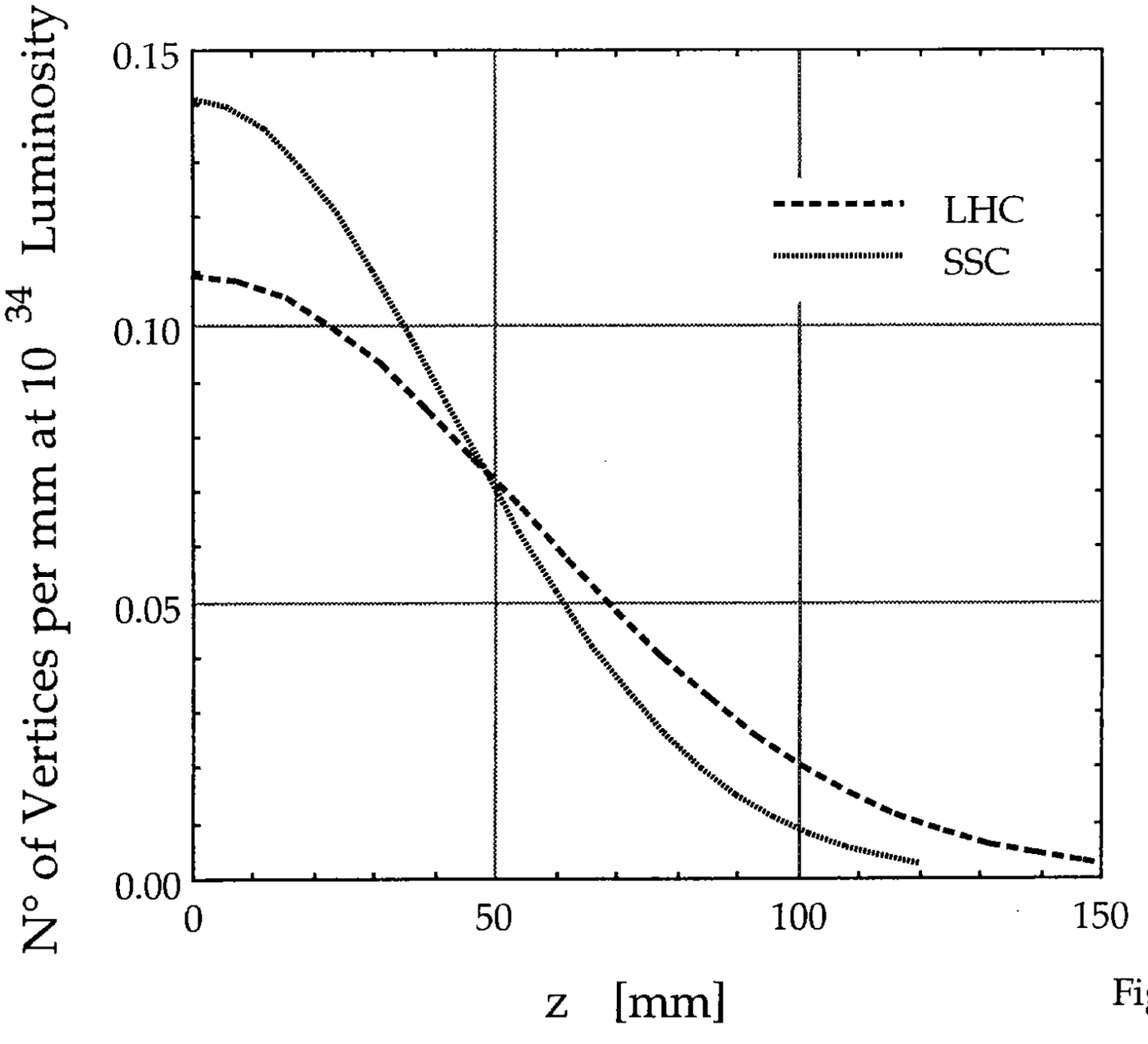
N° of Vertices per mm at 10 34 Luminosity
0.15
0.10
0.05
0.00
0
50
100
150
z [mm]
LHC
SSC

Fig. 1

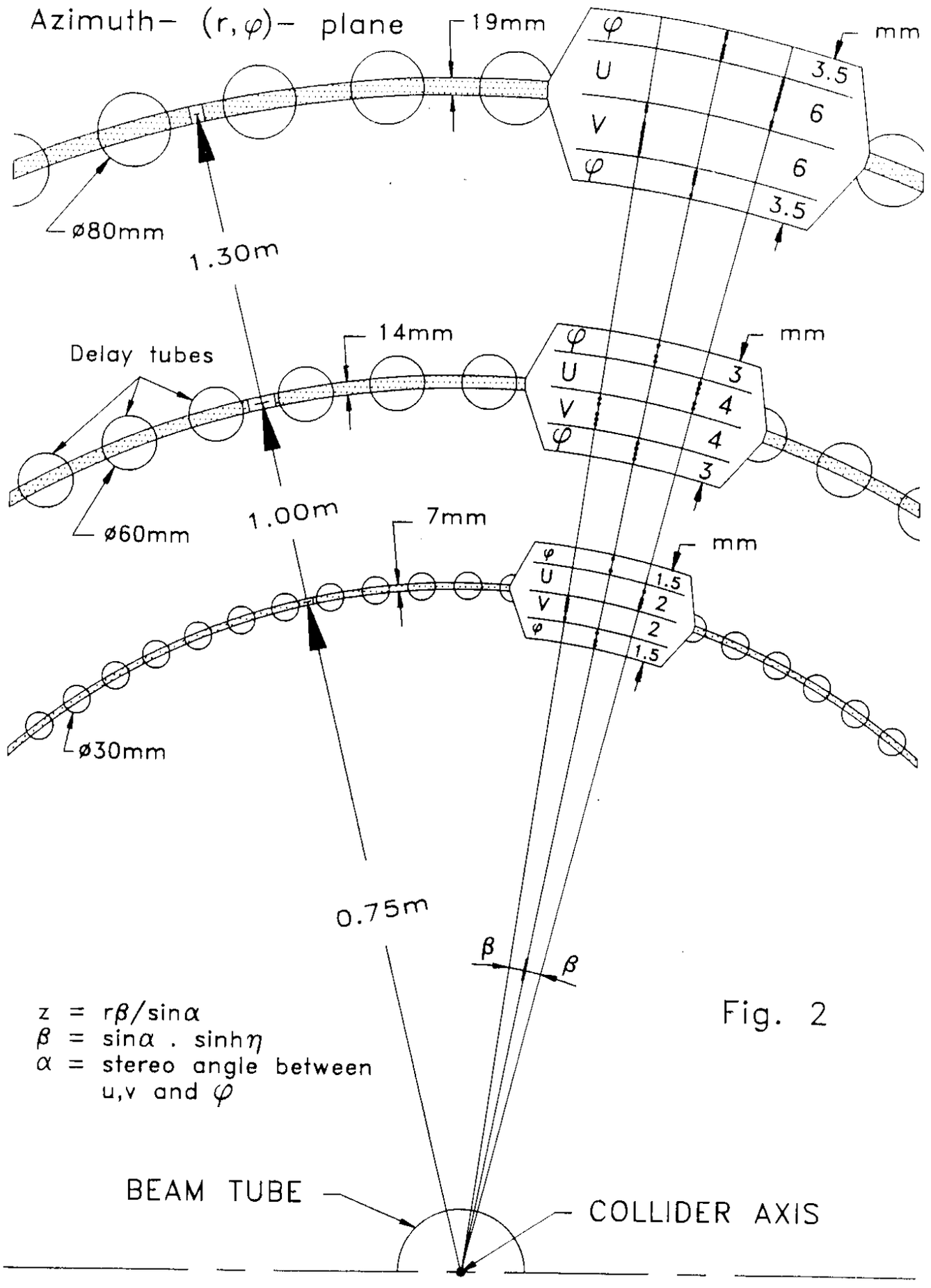
Azimuth– (r, φ)– plane
19mm
mm
φ
U
V
φ
3.5
6
6
3.5
ø80mm
1.30m
Delay tubes
14mm
mm
3
4
4
3
ø60mm
1.00m
7mm
mm
1.5
2
2
1.5
ø30mm
0.75m
β
β
z = rβ/sinα
β = sinα . sinhη
α = stereo angle between u,v and φ
BEAM TUBE
COLLIDER AXIS

Fig. 2

Fig. 3

30 to 60 points per track

r,φ,z – coordinates are measured

~160 millions of fibres are readout by ~400 tubes

which also provide ~1 μs delay for the first level trigger

Polar– (r,z)– plane

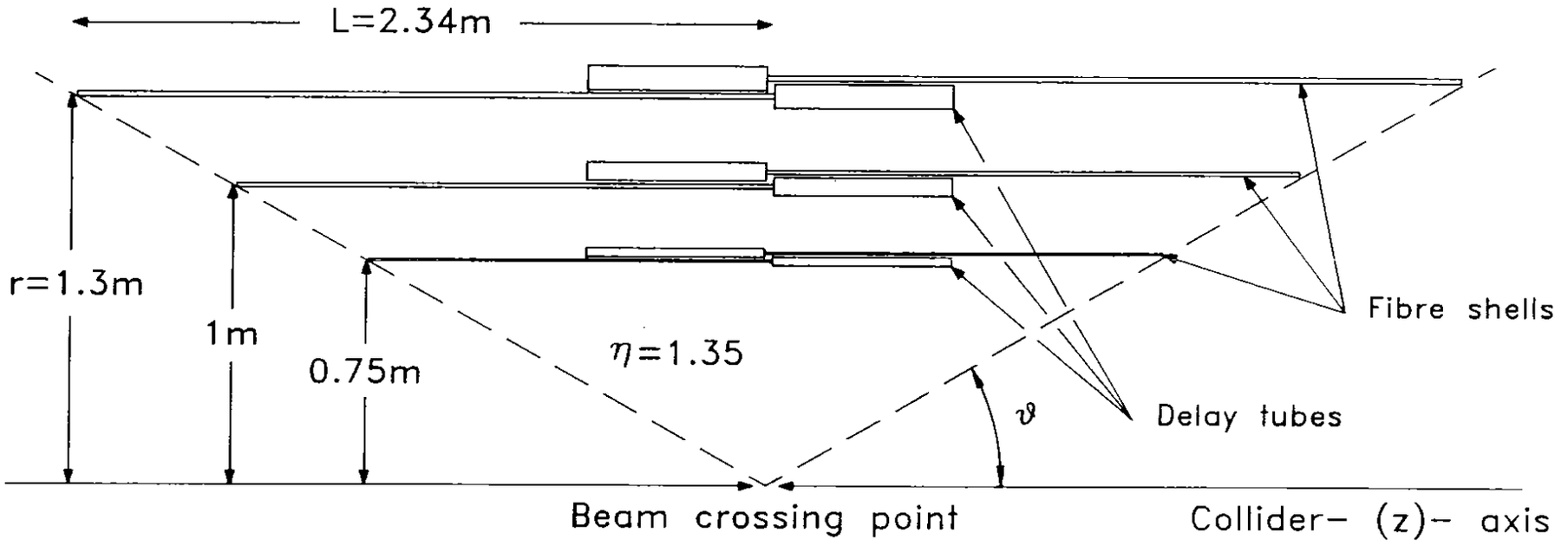

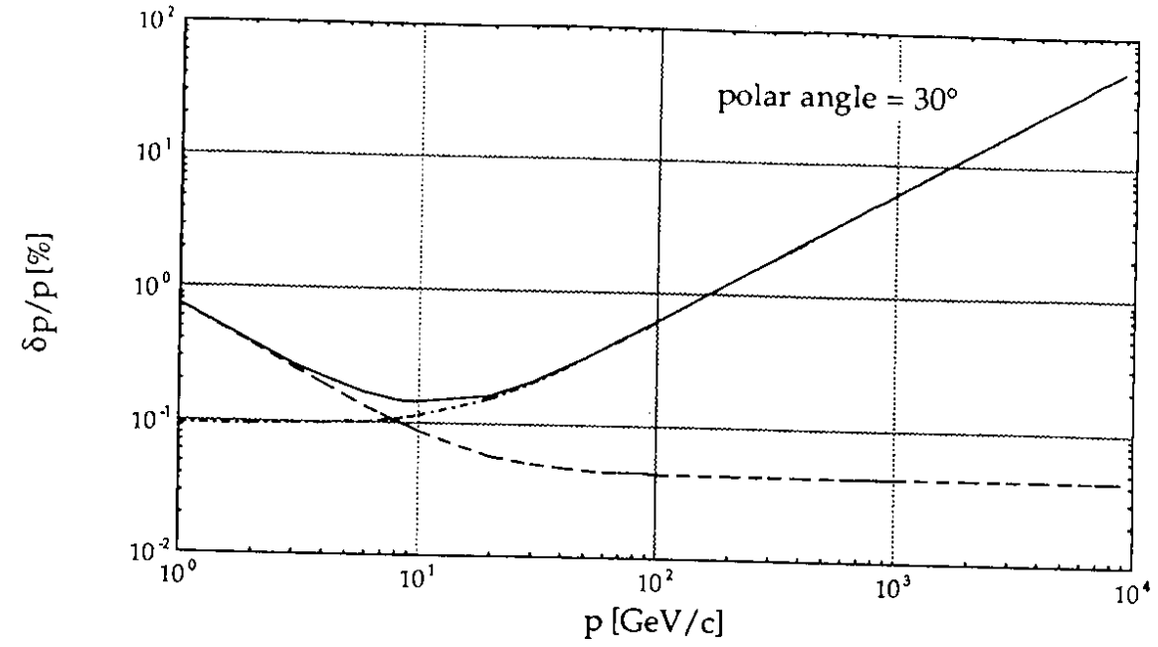
polar angle = 30°
δp/p [%]
p [GeV/c]

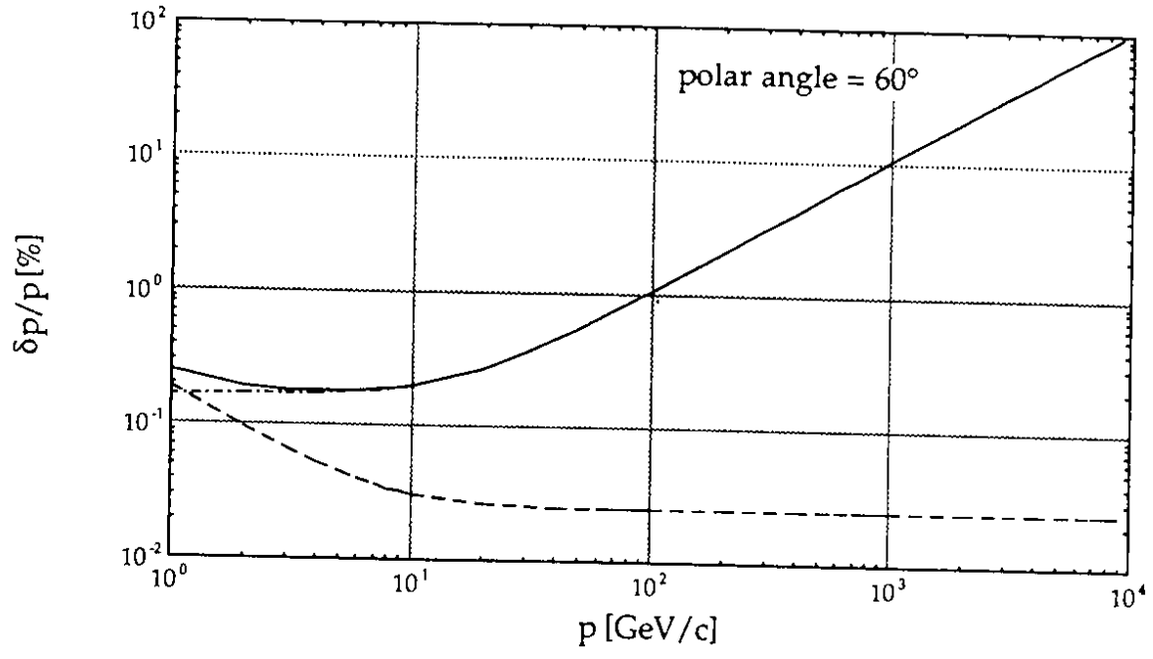
polar angle = 60°
δp/p [%]
p [GeV/c]

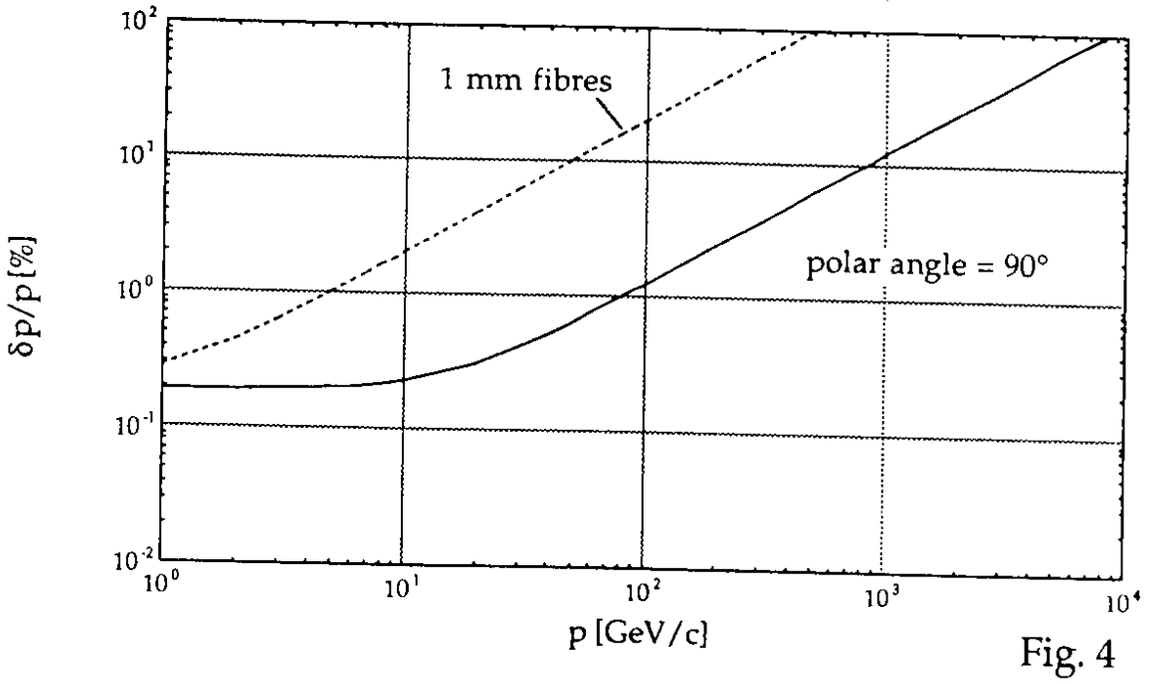
1 mm fibres
polar angle = 90°
δp/p [%]
p [GeV/c]

Fig. 4

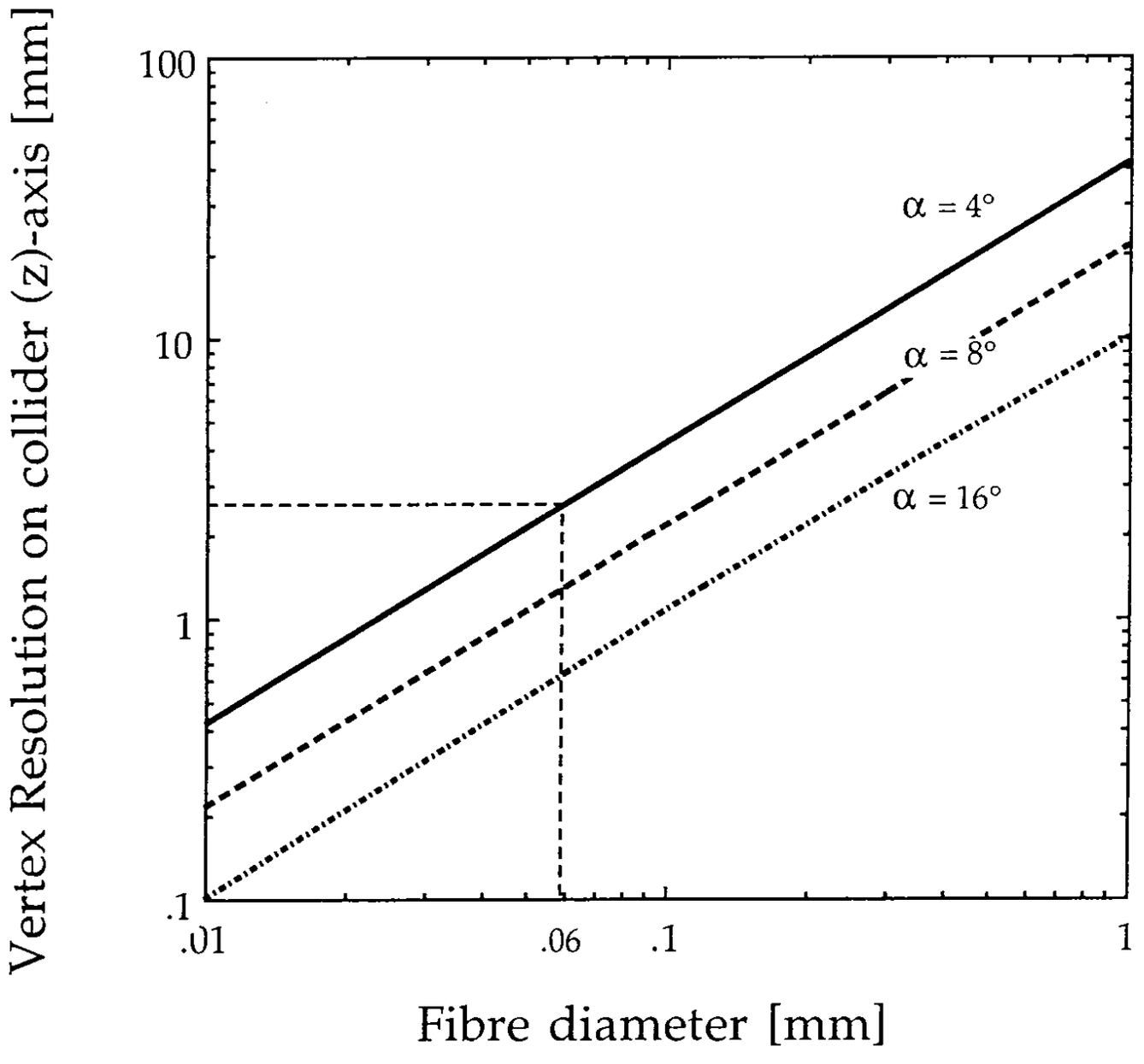
Vertex Resolution on collider (z)-axis [mm]
100
10
1
.1
.01
.06
.1
1
α = 4°
α = 8°
α = 16°
Fibre diameter [mm]

Fig. 5

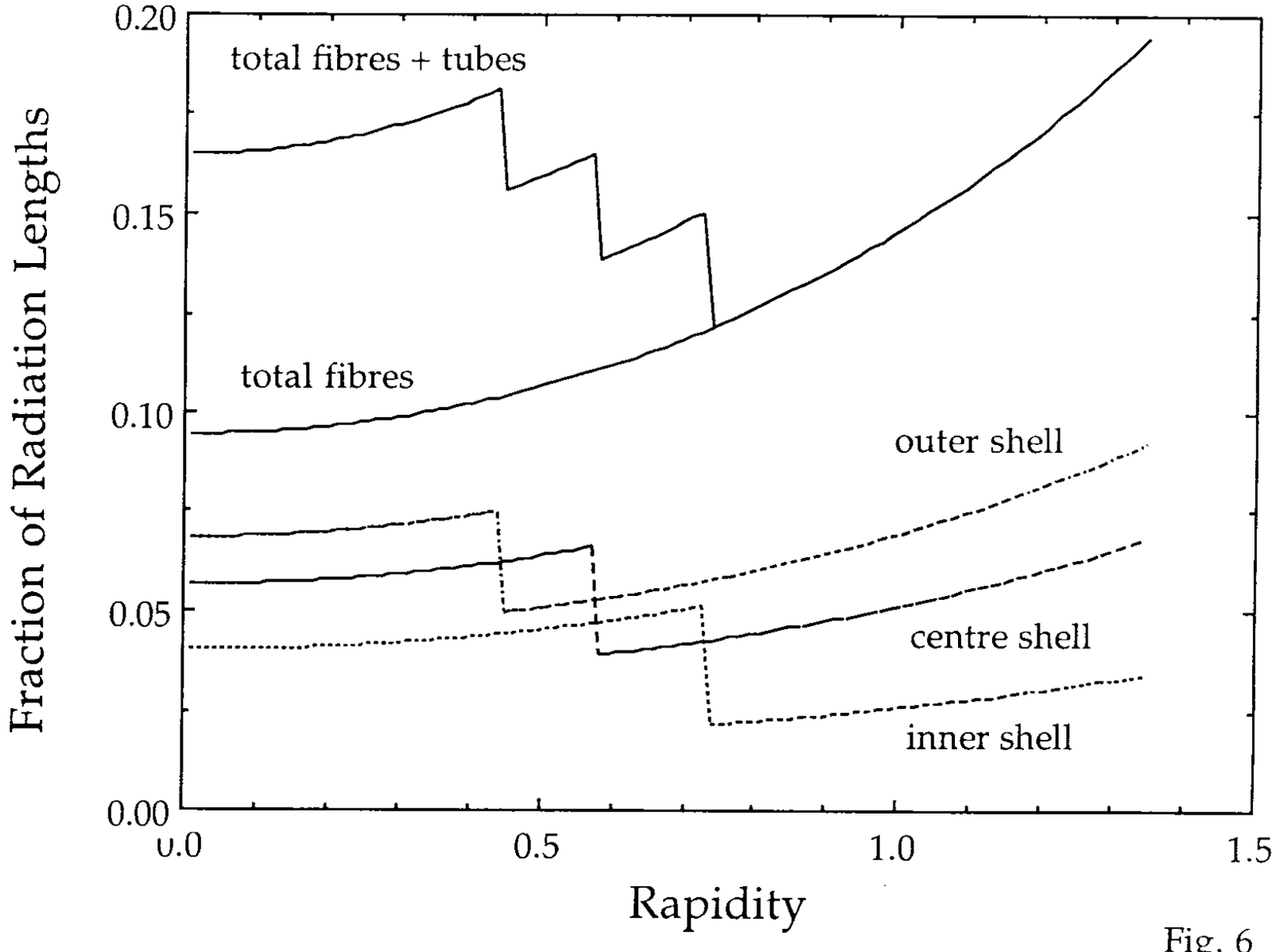
0.20
0.15
0.10
0.05
0.00
0.0
0.5
1.0
1.5
Fraction of Radiation Lengths
Rapidity
total fibres + tubes
total fibres
outer shell
centre shell
inner shell

Fig. 6

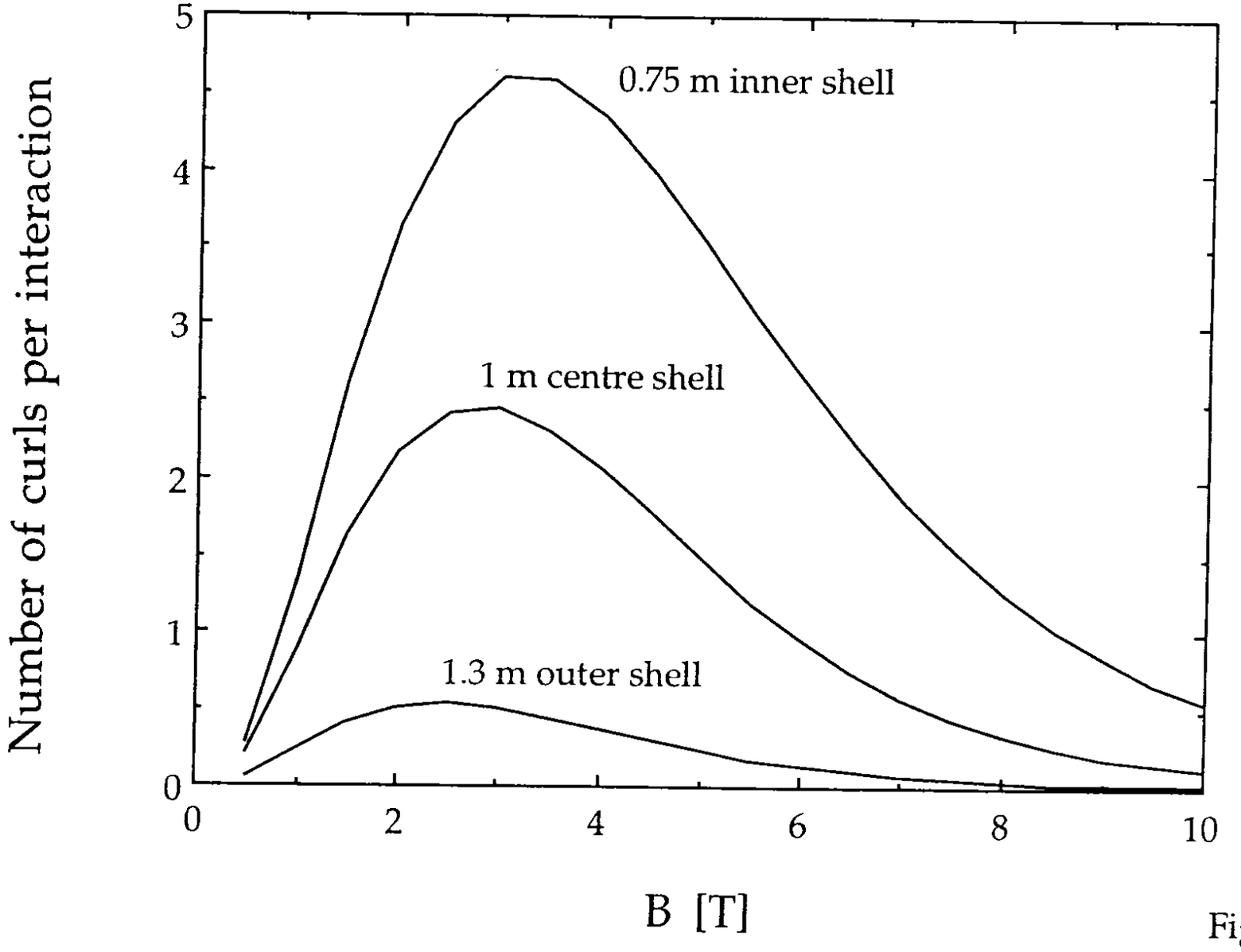
Number of curls per interaction
5
4
3
2
1
0
0
2
4
6
8
10
0.75 m inner shell
1 m centre shell
1.3 m outer shell
B [T]

Fig. 7

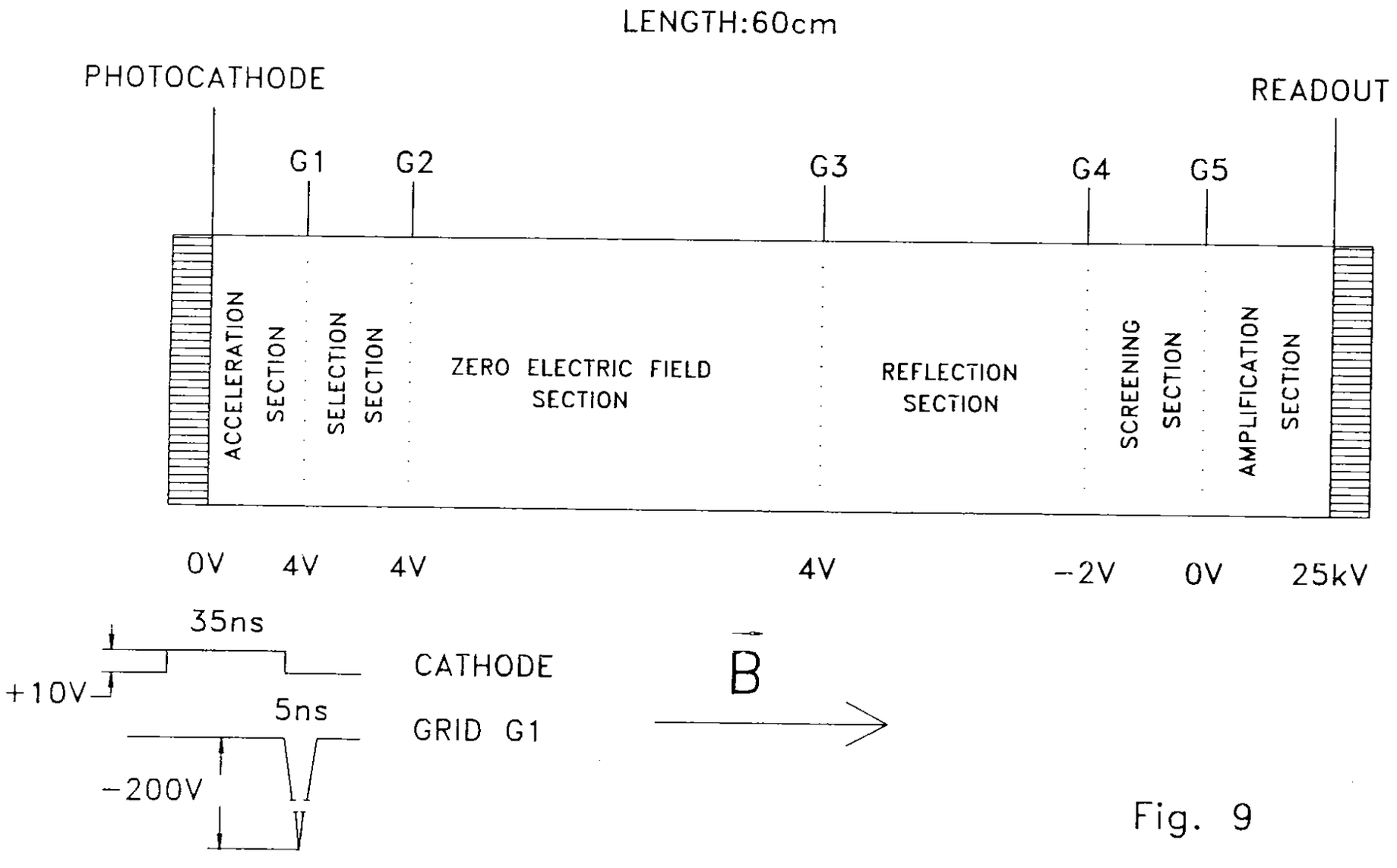
LENGTH:60cm
PHOTOCATHODE
READOUT
G1
G2
G3
G4
G5
ACCELERATION SECTION
SELECTION SECTION
ZERO ELECTRIC FIELD SECTION
REFLECTION SECTION
SCREENING SECTION
AMPLIFICATION SECTION
0V
4V
4V
4V
-2V
0V
25kV
35ns
+10V
CATHODE
5ns
GRID G1
-200V
B

Fig. 9

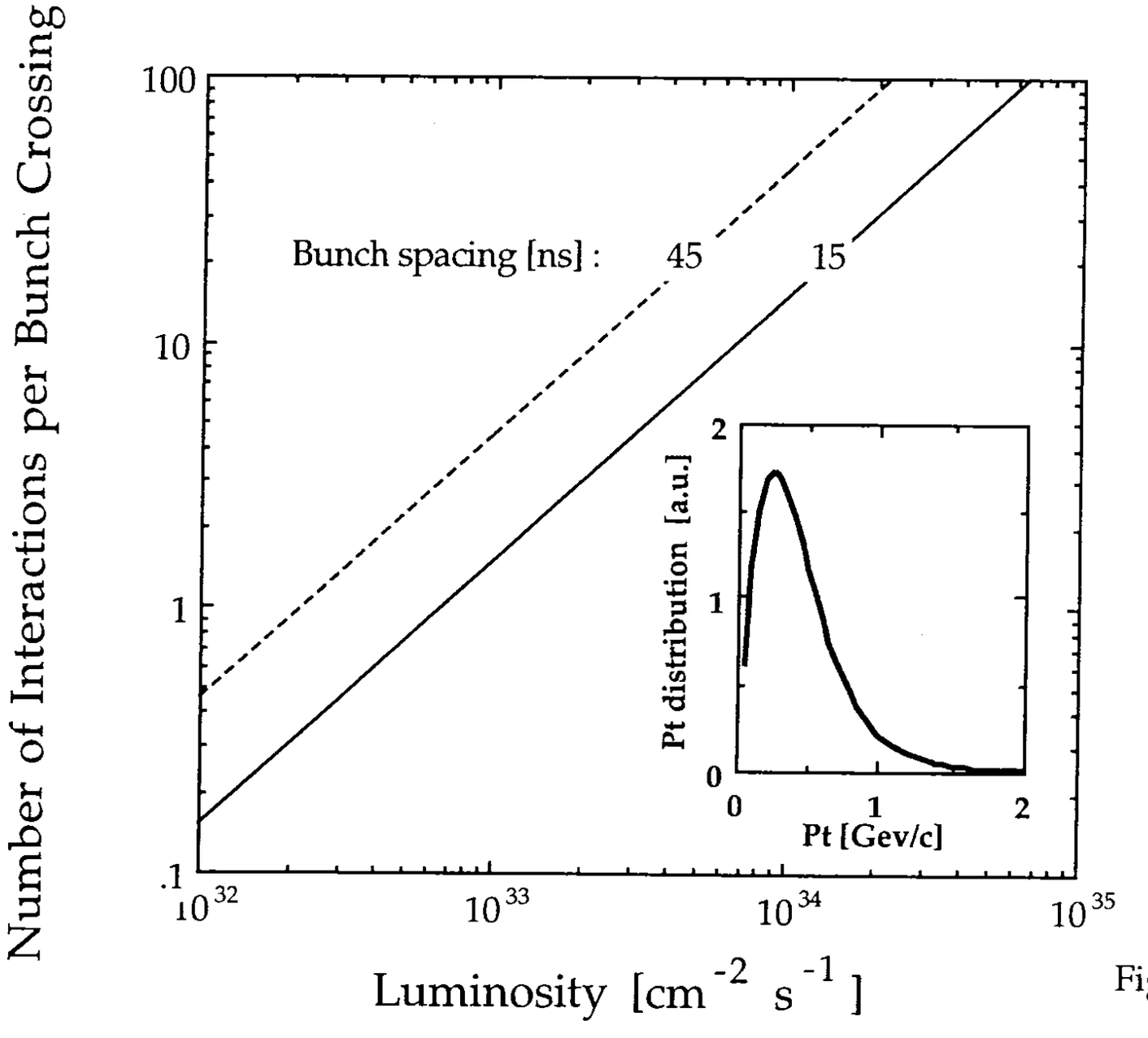
Number of Interactions per Bunch Crossing
100
10
1
.1
Bunch spacing [ns] :
45
15
Pt distribution [a.u.]
2
1
0
0
1
2
Pt [Gev/c]
10^{32}
10^{33}
10^{34}
10^{35}
Luminosity [cm^{-2} s^{-1}]

Fig. 8

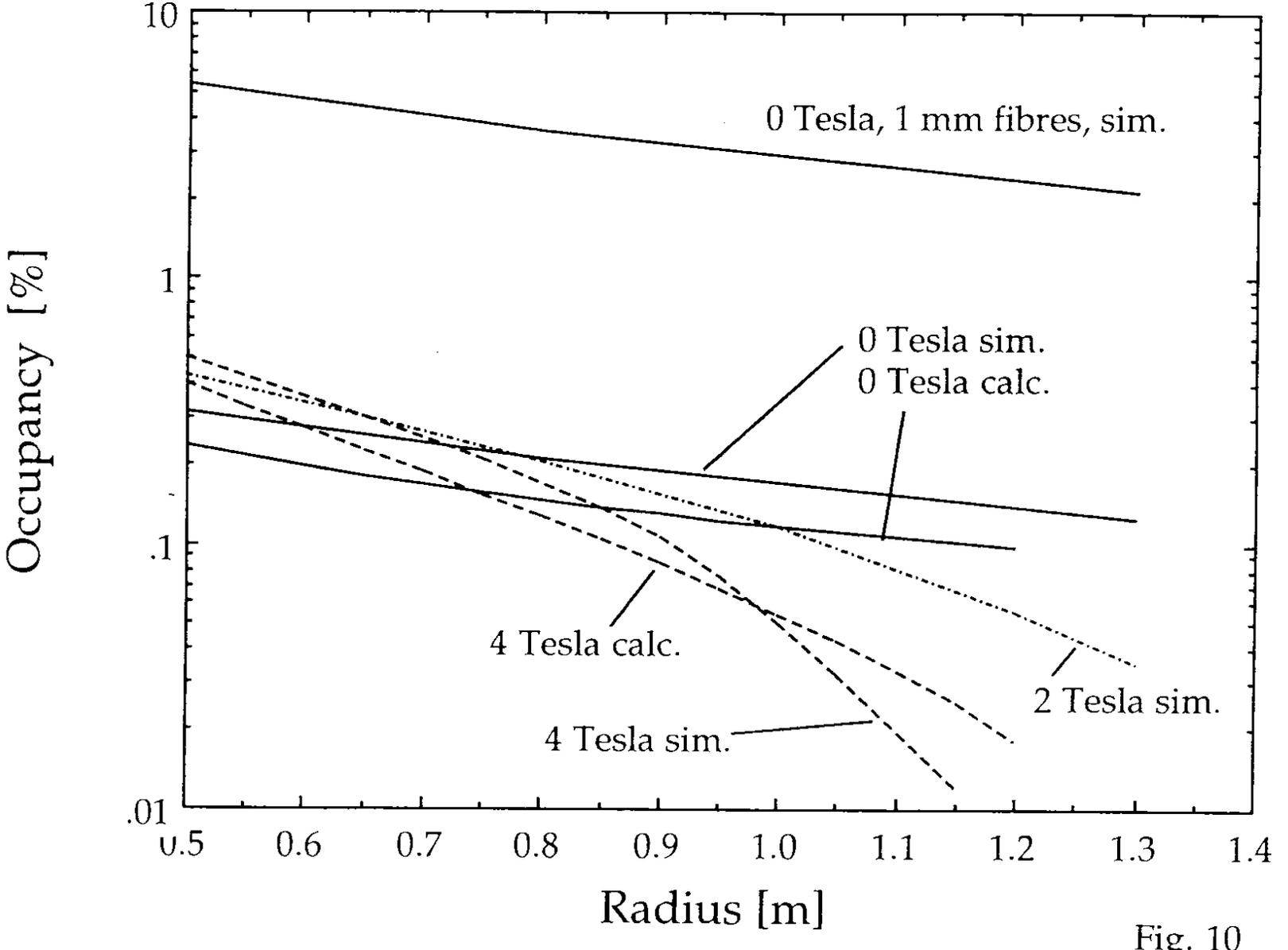
10
1
.1
.01
Occupancy [%]
0.5
0.6
0.7
0.8
0.9
1.0
1.1
1.2
1.3
1.4
Radius [m]
0 Tesla, 1 mm fibres, sim.
0 Tesla sim.
0 Tesla calc.
4 Tesla calc.
2 Tesla sim.
4 Tesla sim.

Fig. 10

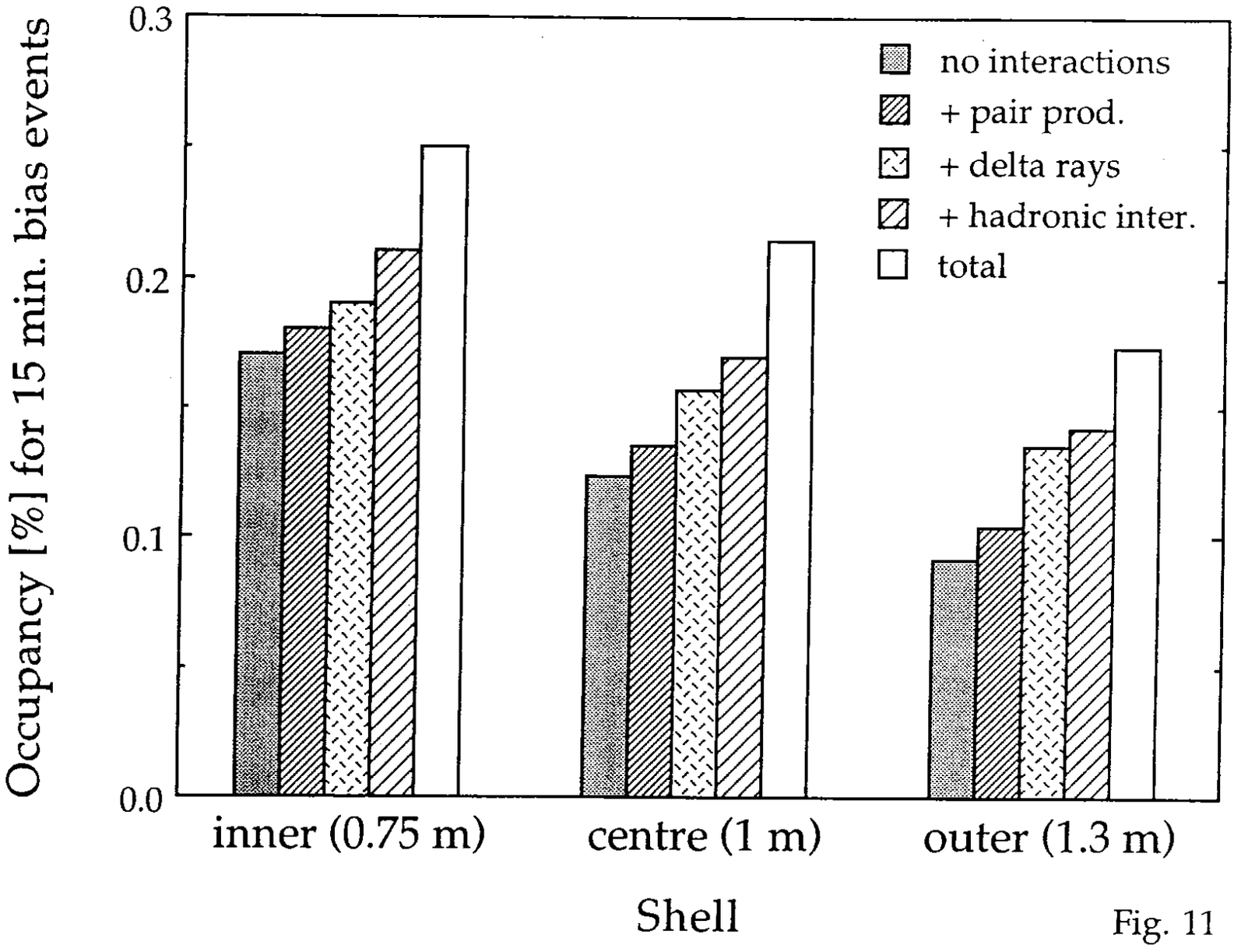
Occupancy [%] for 15 min. bias events
0.3
0.2
0.1
0.0
no interactions
+ pair prod.
+ delta rays
+ hadronic inter.
total
inner (0.75 m)
centre (1 m)
outer (1.3 m)
Shell

Fig. 11

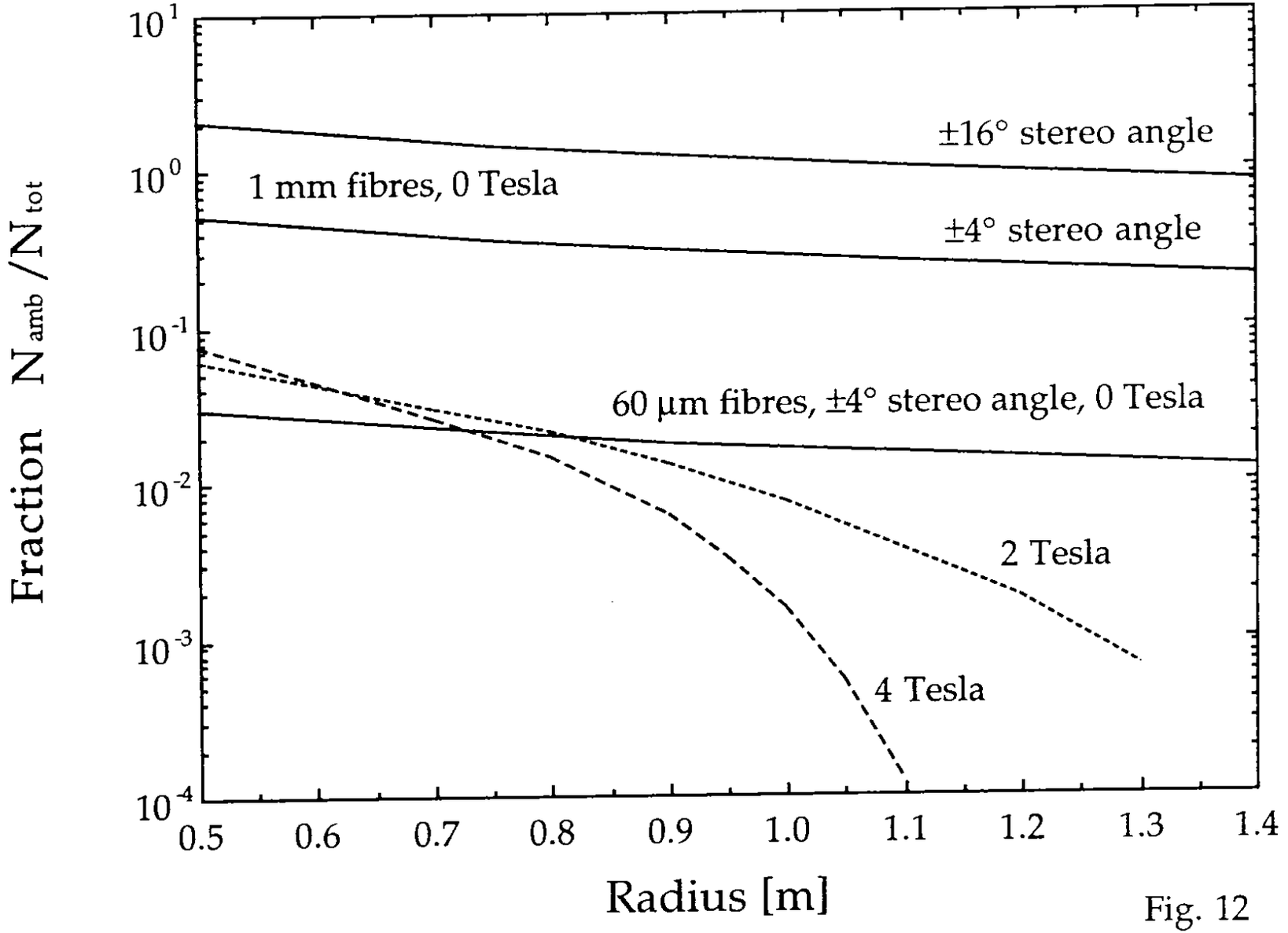
Fraction N_{amb}/N_{tot}
10^{1}
10^{0}
10^{-1}
10^{-2}
10^{-3}
10^{-4}
±16° stereo angle
1 mm fibres, 0 Tesla
±4° stereo angle
60 µm fibres, ±4° stereo angle, 0 Tesla
2 Tesla
4 Tesla
0.5
0.6
0.7
0.8
0.9
1.0
1.1
1.2
1.3
1.4
Radius [m]

Fig. 12